

# Characterization of middle-atmosphere polar warming at Mars

T. McDunn,<sup>1</sup> S. Bougher,<sup>1</sup> J. Murphy,<sup>2</sup> A. Kleinböhl,<sup>3</sup> F. Forget,<sup>4</sup> and M. Smith<sup>5</sup>

Received 5 January 2012; revised 19 October 2012; accepted 18 November 2012; published 11 February 2013.

[1] We characterize middle-atmosphere polar warming (PW) using nearly three Martian years of temperature observations by the Mars Climate Sounder. We report the observed structure of PW and share hypotheses as to possible explanations, which have yet to be tested with global dynamical models. In the data, PW manifested between  $p = 15$  Pa and  $p = 4.8 \times 10^{-3}$  Pa. The latitude where PW maximized shifted poleward with decreasing pressure. The nightside magnitude was larger than the dayside magnitude. The maximum nightside magnitudes ranged from 22 to 67 K. As expected, the annual maximum magnitude in the north occurred during late-local fall to middle-local winter. In the south it occurred during late-local winter. Also as expected, the maximum magnitude near MY 28's southern winter solstice was smaller than that at that same year's northern winter solstice, when a global dust storm was occurring. Unexpectedly, the maximum magnitude at southern winter solstice was comparable to that at northern winter solstice for both MY 29 and MY 30, years that did not experience global dust storms but certainly experienced greater dust loading during  $L_s = 270^\circ$  than  $L_s = 90^\circ$ . Another unexpected result was a hemispheric asymmetry in PW magnitude during most of the observed equinoxes. This paper also provides tables of (1) averaged temperatures as a function of latitude, pressure, and season, and (2) the maximum polar warming features as a function of pressure and season. These tables can be used to validate GCM calculations of middle-atmosphere temperatures and constrain calculations of unobserved winds.

**Citation:** McDunn T., S. Bougher, J. Murphy, A. Kleinböhl, F. Forget, and M. Smith (2013), Characterization of middle-atmosphere polar warming at Mars, *J. Geophys. Res. Planets*, 118, 161–178, doi:10.1002/jgre.20016.

## 1. Introduction

[2] Martian atmospheric polar warming (PW) consists of a temperature enhancement over mid-to-high latitudes during winter, spring, and fall, which results in a reversed (poleward) meridional temperature gradient (e.g., Figure 1). To date, this dynamically induced feature of the Martian atmosphere has not been systematically characterized [Hartogh *et al.*, 2007; Medvedev and Hartogh, 2007].

[3] PW at Mars exhibits similarity to the reversal of the meridional temperature gradient observed in the terrestrial atmosphere above  $\sim 70$  km during solstices, for which the winter-pole mesopause is 70–80 K warmer than the summer-pole mesopause [Holton, 1982]. This reversed terrestrial meridional temperature gradient is maintained dynamically through a thermally direct global circulation with ascent

and adiabatic cooling over the summer polar region and subsidence and adiabatic warming over the winter polar region, as first theorized by Kellogg and Schilling [1951].

[4] The Martian atmosphere also possesses a large-scale thermally direct circulation forced by differential visible and infrared radiation (including suspended dust effects) [Schneider, 1983; Wilson, 1997; Forget *et al.*, 1999] and by atmospheric wave effects [Wilson, 1997; Forget *et al.*, 1999; Hartogh *et al.*, 2007; Medvedev and Hartogh, 2007]. Santee and Crisp [1993] predicted a meridional circulation for the lower Martian atmosphere similar to that proposed for the terrestrial mesosphere by Leovy [1964]. It is not surprising that these similar circulation characteristics might therefore produce similar effects upon higher latitude/polar temperatures. Limited temporal and spatial measurements led early observational studies of Martian polar warming to focus on its winter solstice manifestation [e.g., Deming *et al.*, 1986; Jakosky and Martin, 1987; Théodore *et al.*, 1993; Bougher *et al.*, 2006]. However, Martian PW is not confined to winter latitudes but also manifests during equinoxes over both hemispheres, as first modeled by Forget *et al.* [1999] and later observed by Smith *et al.* [2001] and McCleese *et al.* [2010]. The primary objective of this work is to characterize the magnitude, structure, and seasonality of Martian PW.

### 1.1. Previous Mars PW Investigations

[5] PW was first evident at Mars at middle to high northern latitudes at pressures spanning  $\sim 70$  Pa to the data

All Supporting Information may be found in the online version of this article.

<sup>1</sup>Department of AOSS, University of Michigan, Ann Arbor, Michigan, USA.

<sup>2</sup>Department of Astronomy, NMSU, Las Cruces, New Mexico, USA.

<sup>3</sup>Jet Propulsion Laboratory, California Institute of Technology, Pasadena, California, USA.

<sup>4</sup>LMD, Paris, France.

<sup>5</sup>Sciences and Exploration Directorate, GSFC/NASA, Greenbelt, Maryland, USA.

Corresponding author: T. McDunn, Department of AOSS, University of Michigan, Ann Arbor, Michigan, USA. (tmcdunn@umich.edu)

©2013. American Geophysical Union. All Rights Reserved.  
2169-9097/13/10.1002/jgre.20016

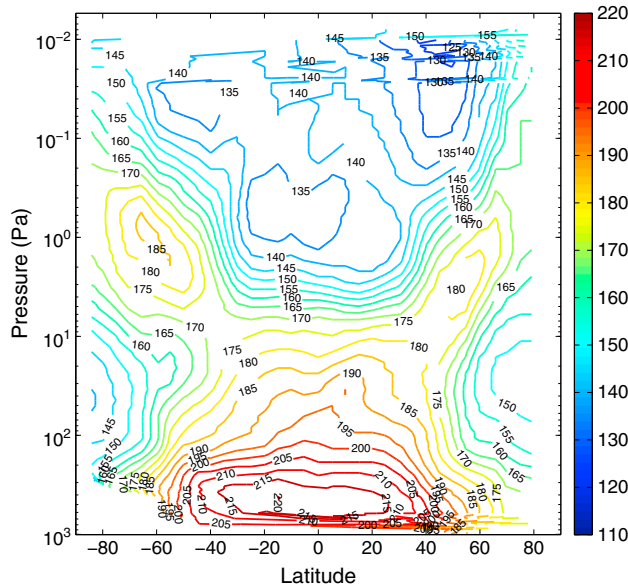


**Figure 1.** Cross-section of middle-atmosphere temperatures as observed by the Mars Climate Sounder during MY 29,  $L_s = 180^\circ \pm 5^\circ$ , LT = 1–5. Contours are drawn every 5 K. Polar warming is visible in both hemispheres above 5 Pa.

limit of 10 Pa during late winter/near equinox ( $L_s$  330–345°) within temperature profiles derived from Mariner 9 IRIS spectra [Conrath *et al.*, 1973; Conrath, 1981]. These conditions existed during the declining phase of the 1971–1972 dust storm. Single-layer atmospheric temperatures centered at 50 Pa derived from Viking IRTM measurements [Martin and Kieffer, 1979] provided evidence of early northern winter polar warming, during dust storm conditions, from which Jakosky and Martin [1987] characterized the spatial and temporal structure of this north polar warming. Deming *et al.* [1986] identified from ground-based disk resolved 10–11  $\mu\text{m}$  spectroscopic observations vertically broad southern hemisphere winter polar warming at lower pressures (0.5–2.0 Pa) during non-dust-storm conditions ( $L_s = 130^\circ$ ). Théodore *et al.* [1993] subsequently obtained vertically resolved temperature profiles in the 0.8–7.0 Pa region from ground-based spectra, which reiterated that PW was present at northern winter latitudes near solstice ( $L_s = 279^\circ$ ), at altitudes higher than those probed by Viking IRTM. Smith *et al.* [2001] presented Mars Global Surveyor/Thermal Emission Spectrometer (TES) retrieved temperatures at pressures between  $\sim 20$  Pa and 0.9 Pa indicating polar warming occurring simultaneously at middle and high latitudes of both hemispheres during  $L_s = 180^\circ$  equinox conditions.

[6] Bougher *et al.* [2006] identified PW in lower thermosphere northern polar winter temperatures derived from Mars Odyssey orbiter aerobraking measurements [Keating *et al.*, 2003; Tolson *et al.*, 2007]. PW was not concurrently evident in lower atmospheric TES-derived temperatures [Smith *et al.*, 2001], nor was PW apparent at thermosphere altitudes at high southern latitudes during southern winter solstice investigated with Mars Global Surveyor aerobraking. Most recently, McCleese *et al.*

[2010] identified PW within Mars Climate Sounder (MCS) derived temperatures centered near 1 Pa at both poles during both equinox seasons.

[7] Numerical investigations have been conducted to understand Martian PW. Barnes and Hollingsworth [1987] demonstrated that a planetary wave mechanism can produce a polar warming exhibiting the magnitude and suddenness detected during the Viking-observed 1977 solstice dust storm. Barnes [1990] and Théodore *et al.* [1993] demonstrated that winter middle latitude gravity wave dissipation is capable of generating PW via its induced polar downwelling. Wilson [1997] illustrated that the large-scale mean meridional circulation could produce PW, but requires that the model top be placed high enough to minimize the effect of model-top friction. This same investigation also indicated that thermal tides contribute a nontrivial role in forcing PW during the simulated dust storm conditions. Hartogh *et al.* [2007], Medvedev and Hartogh [2007], and Kuroda *et al.* [2009] have recently strengthened the argument that atmospheric wave processes (thermal tides, planetary waves, etc.) play an important role in the forcing of Martian PW.

## 1.2. Motivation for this Investigation

[8] Observations of Martian PW prior to the Mars Reconnaissance Orbiter (MRO) mission have offered glimpses of this phenomenon but did not provide sufficient seasonal and vertical coverage from which basic systematic PW characteristics could be determined, such as its: magnitude, vertical and latitudinal structures, seasonality, hemispheric dependence, local time-of-sol dependence, dependence upon atmospheric dust content, and relationship to upper atmosphere PW [e.g., Bougher *et al.*, 2006]. The recently obtained MRO/MCS-derived atmospheric temperatures [McCleese *et al.*, 2007; Kleinböhl *et al.*, 2009] provide an unprecedented vertical thermal structure of the lower and middle atmosphere, extending from the surface to  $\sim 80$ –90 km. These temperature data are used here to characterize the magnitude, structure, and seasonality of Martian PW. This characterization is the primary objective of this study.

[9] The second objective of this study is to provide tabulated observational constraints for numerical calculations of atmospheric fields, including polar warming, in the Martian middle atmosphere ( $p = 10$  to  $1 \times 10^{-4}$  Pa corresponding roughly to 30 to 120 km altitude). This follows the philosophy of Jakosky and Martin’s [1987] characterization of the Viking-observed lower-atmosphere 1977 (MY 12) north polar warming. There has to date been a shortage of constraints for middle-atmosphere calculations, save those provided by the Spectroscopy for Investigation of Characteristics of the Atmosphere of Mars (SPICAM) data set [Forget *et al.*, 2009; McDunn *et al.*, 2010]. As noted by Hartogh *et al.* [2007], “Existing observations cannot definitely validate the magnitude and location of the martian winter polar warmings, [or] constrain general circulation models.” In response to this need for middle-atmosphere constraints, this paper provides a set of tabulated MCS temperatures for the validation and constraint of GCM middle-atmosphere calculations (see the Supporting Information).

[10] In section 2, we briefly describe the MCS and SPICAM temperature data sets, including our data binning strategy for PW characterization. In section 3, we present

the PW quantification methodology and discuss the observed middle-atmosphere PW, including its spatial, diurnal, seasonal, and interannual trends and variabilities. In section 4, we present quantitative constraints for GCM middle-atmosphere calculations. Finally, in section 5, we summarize this work and offer perspectives for future studies.

## 2. Temperature Data Sets From $p = 10$ Pa to $1 \times 10^{-4}$ Pa From Spacecraft

[11] The nominal spatial and temporal coverage provided by the data sets is shown in Table 1. The MCS data are the primary data for the PW characterization; the SPICAM data are explored where and when available in an attempt to vertically extend the MCS characterization.

### 2.1. Mars Climate Sounder

[12] MCS is a passive infrared radiometer measuring thermally emitted radiation in both limb and on-planet geometries [McCleese *et al.*, 2007]. From these measurements, vertical profiles of pressure and temperature are retrieved using a modified Chahine method and the Curtis-Godson approximation [Kleinböhl *et al.*, 2009, 2011]. Vertical resolution of the individual retrievals is  $\sim 5$  km with  $\sim 2$  K temperature uncertainties [Kleinböhl *et al.*, 2009, 2011]. Retrieved pressures and temperatures from MCS' 21 instantaneous limb fields-of-view are interpolated to a fixed set of 105 pressure levels ranging from the surface up to  $4.8 \times 10^{-3}$  Pa ( $\sim 80$ – $90$  km altitude). The highest altitude at which pressures and temperatures are retrieved (the profile's "topside") depends upon instrument pointing and high altitude temperature (signal-to-noise). An MCS pointing restriction during Mars Year (MY) 28,  $L_s = 181$ – $258^\circ$  prevented MCS from tracking the limb, resulting in southern hemisphere topsides that were lower altitude than usual ( $\sim 50$  km altitude) and northern hemisphere topsides that were higher altitude than usual ( $\sim 90$  km altitude) (see Figures 6G–L and 7A–C). MCS data have inferior calibration during this period. The MCS data employed for this investigation are from the Version 3 retrieval process, for which on-planet views have been incorporated with limb views to produce profiles extending to near the surface.

[13] MCS has operated nearly continuously since September 2006. Sparse coverage during the dust seasons (Figure 2a), particularly during the global dust storm of 2007 (MY 28,  $L_s = 265$ – $300^\circ$ ), is due to airborne dust scattering obscuring the instrument's view. Global data dropouts (e.g., MY 29,  $L_s = 328^\circ$  to MY 30,  $L_s = 23^\circ$ ) are a result of instrument stowing due to spacecraft or instrument anomalies. The Sun-synchronous nature of MRO's orbit dictates that MCS repeatedly observes the atmosphere at two local times,

3 A.M. and 3 P.M., except near the poles, where the observed local times are more extensive (Figure 2b).

[14] Previous analyses of MCS temperatures have revealed the zonal mean thermal structure and its variability from near the surface to 80–90 km altitude. McCleese *et al.* [2010] identified an equatorially symmetric equinoctial thermal structure and an equatorially asymmetric solstitial thermal structure. McCleese *et al.* [2008, 2010] identified PW during solstices and McCleese *et al.* [2010] identified PW during equinoxes. Lee *et al.* [2009] examined thermal tides and found most diurnal variations in temperature were associated with the diurnal thermal tide. Heavens *et al.* [2010] investigated dry convective instabilities in the middle-atmosphere and found them to be widespread across the planet and largest over the northern winter extratropics. Finally, Heavens *et al.* [2011] studied the kinematic coupling between the mean meridional circulation of the lower and middle atmosphere.

### 2.2. Spectroscopy for Investigation of Characteristics of the Atmosphere of Mars

[15] SPICAM is a dual spectrometer that performs stellar occultations in the 110–310 nm (UV) and 1.0–1.7  $\mu$ m (near-IR) bands [Quémerais *et al.*, 2006]. Neutral density profiles are extracted from UV observations between altitudes of 50–140 km at a vertical resolution of 1–2 km [Quémerais *et al.*, 2006; Bertaux *et al.*, 2006]. Forget *et al.* [2009] used the derived density scale heights to derive neutral temperature profiles between altitudes of  $\sim 70$  km and  $\sim 120$  km. Temperature profile vertical resolution is 1–2 km with uncertainties on the order of 3–15 K (smaller errors at 120 km altitude) [Forget *et al.*, 2009].

[16] During MY 27, SPICAM accumulated 616 profiles [Forget *et al.*, 2009], most from the fall and winter hemispheres (Figure 3b) due to the nonuniform distribution of UV stars across the sky [Quémerais *et al.*, 2006]. Most observations are from Mars' nightside (LT = 1800–0600) (Figure 3c) to avoid contamination from scattered and reflected sunlight [Forget *et al.*, 2009].

[17] Previous investigations of SPICAM temperatures have indicated mesopause temperatures below the CO<sub>2</sub> frost-point, primarily in the southern winter tropics [Montmessin *et al.*, 2006; Forget *et al.*, 2009], moderate ( $\sim 20$ – $30$  K) nightside PW from  $p = 1 \times 10^{-1}$  to  $1 \times 10^{-2}$  Pa during southern winter ( $L_s = 90$ – $120^\circ$ ) [Forget *et al.*, 2009], and seasonal and spatial variability in the temperature and pressure of the nightside mesopause [McDunn *et al.*, 2010].

[18] In this study we attempted to investigate the overlap between PW in the MCS and SPICAM datasets, but found it yielded no new results not already presented in Forget *et al.* [2009]. We found the PW present in the MY 27 SPICAM data set is limited to that discussed earlier ( $L_s = 90$ – $120^\circ$ , at  $p = 0.01$  to 0.1 Pa). As seen in the SPICAM PW figure in the Supporting

**Table 1.** Nominal Domains for the Temperature Data Sets Used in This Study

Instrument	# Profiles	MY	$L_s$ ( $^\circ$ )	F10.7-cm at Earth	LT (h)	Latitude ( $^\circ$ N)	Pressure (Pa)
MCS	$> 2e+6$	28	111–360	70–110	1–5, 13–17	–85 to 85	$1e+1$ to $4e-3$
		29	0–360				
		30	0–360				
SPICAM	616	27	0–360	70–130	mostly 18–06	mostly fall and winter	$1e-1$ to $1e-4$

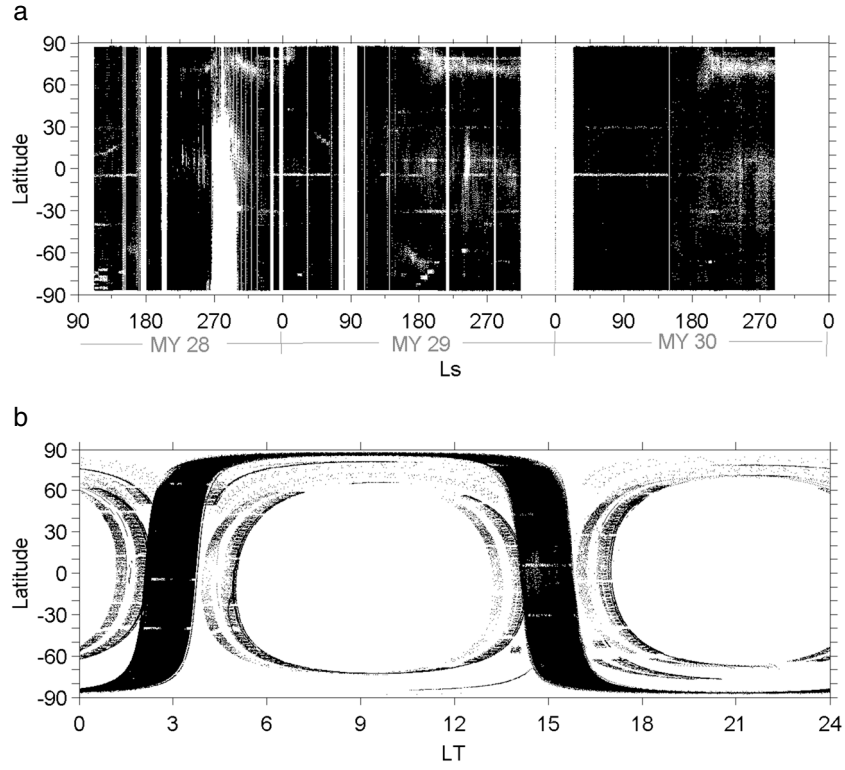


**Figure 2.** (a) Seasonal and (b) local time distribution of MCS Version 3 temperature retrievals.

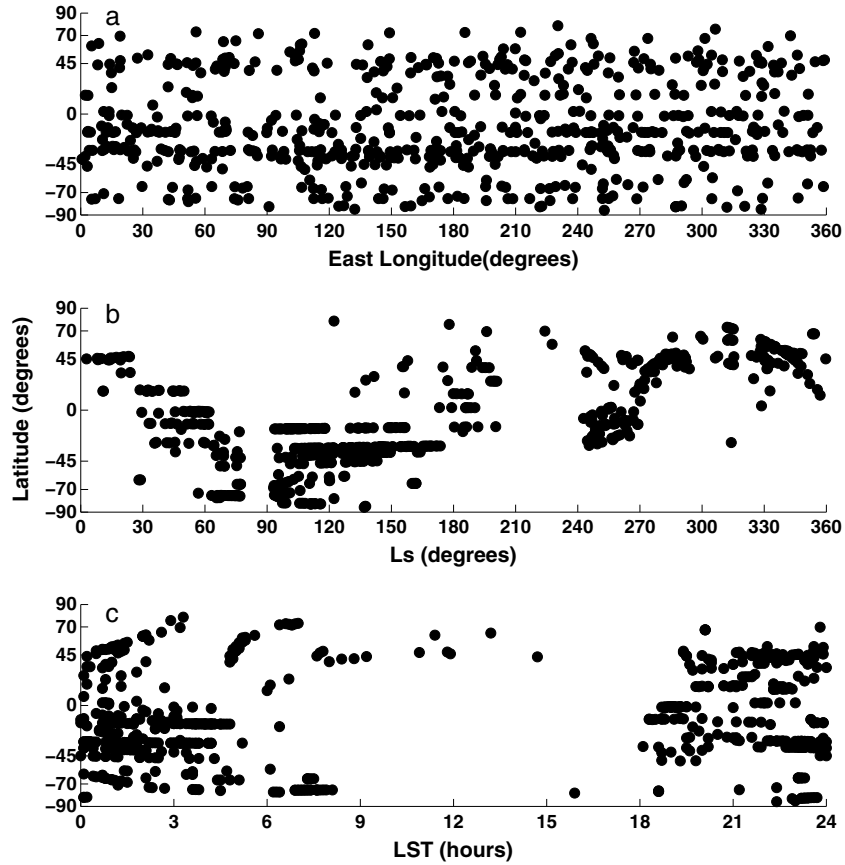


**Figure 3.** (a) Horizontal, (b) seasonal, and (c) local time distribution of SPICAM temperatures.

Information, insufficient coverage, especially at high latitudes, renders the presence or absence of PW at other seasons inconclusive at this point. However, this situation may change with the addition of two more MYs of SPICAM data (MY 28 and MY 29), which are anticipated to be released in the near future.

### 2.3. Data Binning

[19] In this presentation PW is characterized from spatially and temporally binned MCS temperatures on each pressure surface. Temperatures are binned in season (i.e.,  $L_s = 0-10^\circ$ ,  $10-20^\circ$ ,  $20-30^\circ$ , ...,  $350-360^\circ$ ) and Local Time (LT) (“nightside” = 0100 to 0500, “dayside” = 1300 to 1700), in addition to being zonally binned (averaged). SPICAM temperatures are binned in broader LT bins (“nightside” = 1900 to 0500 and “dayside” = 0700 to 1700) to improve the sampling. Temperatures on each pressure surface are also binned by latitude ( $0^\circ \pm 2.5^\circ$ ,  $5^\circ \pm 2.5^\circ$ , etc.). The result of the binning is time and zonally averaged temperatures for each pressure-season-LT-latitude bin. Standard deviations for most bins are  $< 15$  K, with the exceptions occurring during northern winter when some bins have standard deviation values as large as 30 K. In accordance with the MCS temperature retrieval technique, which relaxes the profile to isothermal when the error exceeds 5% [Kleinböhl et al., 2009] (which typically occurs near 80 km altitude where the global-average temperature is approximately 140 K), bin-averaged temperatures having propagated error  $\geq 7$  K are discarded and not included in the procedure for identifying PW. PW magnitude and structure are identified from the remaining bin-averaged temperatures (see section 3). For the purpose of this paper, we use a high-latitude temperature enhancement (see equation (1)) of 15 K as the threshold for identifying PW. A sample of the observed temperatures and the bin-average curves versus latitude for select pressure surfaces and seasons is shown in Figure 4.

### 3. PW Quantification Results and Discussion

[20] Martian atmospheric PW consists of a temperature enhancement over middle- to high-latitude during winter, spring, and fall, which results in a reversed (poleward) meridional temperature gradient on surfaces of constant pressure. Our philosophy here is to develop a data-based characterization of PW. Our procedure for identifying and quantifying PW as a function of pressure and latitude is as follows: on each pressure surface, we locate the largest bin-average temperature in each hemisphere,  $T_1$  (see Figure 5). Then, we locate  $T_2$ , the smallest bin-average temperature between  $Lat_{T_1}$  (latitude of  $T_1$ ) and the equator. The temperature enhancement is then calculated at every ( $5^\circ$ ) latitude bin,  $Lat$ , as

$$\Delta_p T(Lat) = [T_{Lat} - T_2]_p, \quad Lat_{T_2} < Lat \leq Lat_{T_1}. \quad (1)$$

[21] This quantification serves two purposes: (1) it quantifies the dynamically enhanced temperatures as a function of pressure and latitude and (2) it provides a quantifiable constraint for models. In addition, the latitude where  $T_1$  occurs is likely to be an indicator of the region of the

meridional circulation’s descending branch. Tabulations of these results (see Table 2) are provided in the Supporting Information as a resource for straightforward comparisons with simulations.

[22] Other considerations for a data-based PW quantification included

$$\Delta_p T = [T_1 - T_{equator}]_p \quad (2)$$

where  $T_{equator}$  is the bin-average temperature at the equator,

$$\Delta_p T = [T_{winterpole} - T_{summerpole}]_p \quad (3)$$

where  $T_{winterpole}$  and  $T_{summerpole}$  are the bin-average temperatures at the winter and summer poles, respectively,

$$\Delta_p T = [T_1 - T_{fixed\ latitude}]_p \quad (4)$$

where  $T_{fixed\ latitude}$  is the bin-average temperature at a fixed chosen latitude, and the average meridional temperature gradient over the latitudes of enhanced temperature

$$\nabla_p T = [T_1 - T_2]_p / [Lat_{T_1} - Lat_{T_2}]_p \quad (5)$$

[23] Equation (1) is advantageous for a multiseason characterization of PW because it: (1) is not inherently biased toward producing higher magnitudes at equinoxes (which would occur with equation (2), for instance) or solstices (which would occur with equation (3), for instance) and (2) is easily comparable to definitions used in recent studies [Bougher et al., 2006; Hartogh et al., 2007; Forget et al., 2009; González-Galindo et al., 2009a, 2009b]. A disadvantage of this index is that it does not readily lend itself to comparison with the quantifications of PW employed in early studies [e.g., Deming et al., 1986; Théodore et al., 1993] (which could be achieved with equation (5)). Given these points, we found equation (1) to be the most illustrative and useful quantification metric.

[24] An alternative philosophy toward the quantification of PW is to compute the enhancement above radiative-equilibrium temperature at each location

$$\Delta T(p, lat) = T_{ob}(p, lat) - T_{rc}(p, lat) \quad (6)$$

where  $T_{ob}$  is the bin-average observed temperature and  $T_{rc}$  is the bin-average temperature computed by a radiative-convective model. While this method represents the true polar warming (i.e., the dynamically-generated enhancement above radiative equilibrium and the  $CO_2$  saturation vapor pressure constraint), it necessarily introduces into the polar warming determination assumptions about and sensitivity to the aerosol distributions, which are not necessarily well characterized by the currently available observations. Mars GCM simulation results comparing radiative convective saturation temperatures to dynamically influenced temperatures (not shown) suggest that PW as characterized by equation (1) does generally capture the latitude versus pressure structure of the polar warming, which arises from equation (6), though the maximum warming tends to occur at somewhat lower pressure when equation (1) is employed. The magnitude of warming is larger (10–20%) when equation (6) is applied, with this effect being more prominent at the solstices. For the moment, we favor the data-based determination of polar warming as characterized

by equation (1). Improvements in the knowledge of aerosol content will in time result in equation (6) being an improved tool. PW magnitudes discussed from this point forward refer to those calculated via equation (1).

[25] Sections 3.1–3.3 characterize the observed nightside PW (Figures 6–14). Section 3.4 summarizes the differences observed on the dayside (Plots of the dayside PW are found in the Supporting Information).

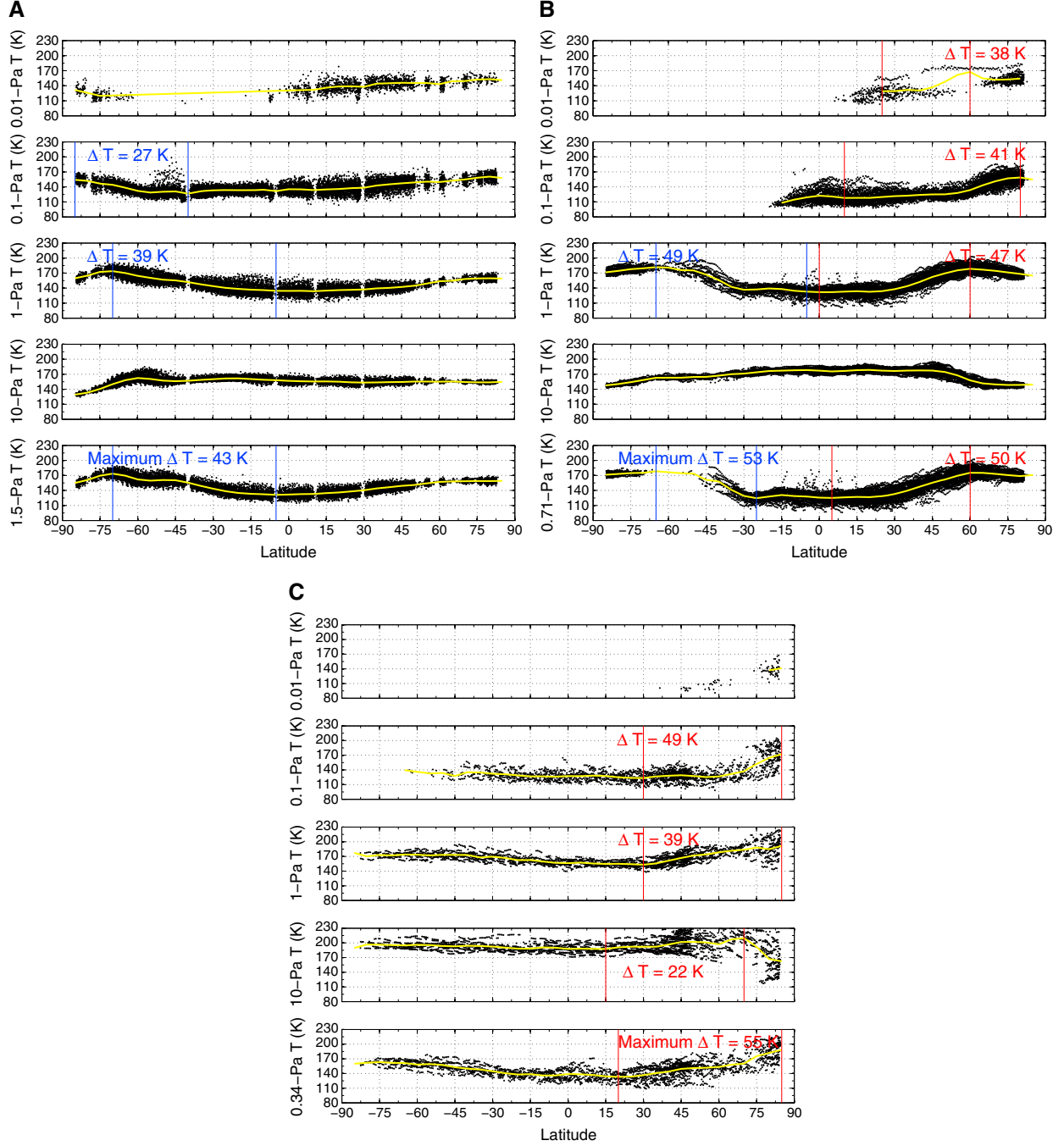


**Figure 4.** Nightside MCS temperatures versus latitude on select pressure surfaces for MY 28: (A) near southern winter ( $L_s = 115^\circ$ ), (B)  $L_s = 180^\circ$  equinox, and (C) northern winter ( $L_s = 270^\circ$ ). Black points depict temperatures from MCS. The yellow curve is the  $5^\circ$  latitude bin-average. The latitudes of  $T_1$  and  $T_2$  are traced by solid blue lines in the southern hemisphere and solid red lines in the northern hemisphere. The maximum PW magnitude on each pressure surface is printed. The pressure surfaces displayed in the top four subpanels are consistent across all seasons ( $p = 10, 1, 0.1$ , and  $0.01$  Pa), while that displayed in the bottom subpanel varies with season to depict the pressure surface on which PW maximizes. During equinox, the pressure surface shown in the bottom subpanel is chosen based on the hemisphere that has the greater maximum  $\Delta_p T$  during that season.



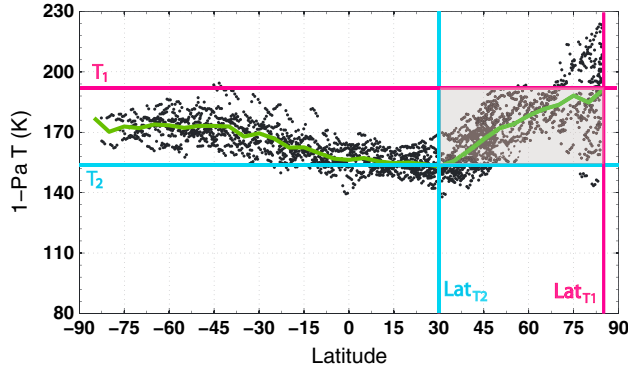


**Figure 5.** Example demonstrating the procedure for computing the metric defined in equation (1). The black points represent individual MCS observations on the  $p=1$  Pa surface during this northern winter season. The green curve corresponds to the bin-averaged temperatures. First, the greatest bin-averaged temperature,  $T_1$ , is identified (indicated by the red crosshairs). Then, the smallest bin-averaged temperature between equator and  $Lat_{T1}$ ,  $T_2$ , is identified (indicated by the blue crosshairs).  $\Delta_p T(Lat)$  values are then calculated for each  $5^\circ$  latitude bin,  $Lat$ , between  $Lat_{T2}$  and  $Lat_{T1}$  (grey-shaded region).

### 3.1. Vertical Range of PW

[26] The bottom extent of PW ranged from  $p=1.1$  to  $15$  Pa ( $\sim 25$ – $50$  km altitude) (e.g., Figures 13F and 7F, respectively) and tended to occur at middle latitudes, rising toward the poles. These bottom extents are consistent with *Santee and Crisp's* [1993] observations of northern-winter PW at  $p \sim 10$  Pa. The top extent of PW ranged from the data limit of  $p=4.8 \times 10^{-3}$  Pa to  $p=1.0 \times 10^{-1}$  Pa ( $\sim 65$ – $90$  km altitude) (e.g., Figures 6G and 7G, respectively) and tended to occur at high latitudes, falling off toward the equator (Note that from MY 28,  $L_s=181^\circ$  to MY 28,  $L_s=258^\circ$  there was an MCS pointing restriction that led to higher than usual observations in the northern hemisphere and lower than usual observations in the southern hemisphere (section 2.1). This explains the unusually low top extents of PW in the southern hemisphere in Figures 6G through 7C.). The top extent was frequently slightly (e.g., Figure 6E) or

significantly (e.g., Figure 11D) higher in the northern hemisphere than in the southern hemisphere. These top extents corroborate past modeling studies that found that a model domain up to at least  $90$  km altitude was necessary to capture the full circulation and simulate middle-atmosphere PW [Wilson, 1997; Forget et al., 1999]. During the global dust storm of MY 28 (see Figure 15), PW penetrated to greater pressures (lower altitudes) (Figures 7D–7H) than during prior or subsequent seasons. Such a downward penetration was not evident during the same season of either MY 29 (Figures 10D–10H) or MY 30 (Figures 13D–13F), when there was no global dust storm activity (see Figure 15). Greater downward penetration under global dust storm conditions is consistent with the PW manifest in the Viking IRTM temperatures during the early northern winter dust storm in 1977 (MY 12) [Jakosky and Martin, 1987].

### 3.2. Latitudinal Range of PW

[27] PW manifested between  $\sim 25^\circ$  (Figure 8A) and  $85^\circ$  latitude (e.g., Figure 6A). As mentioned above, the bottom extent occurred at middle latitudes. Above this, throughout much of the year, the latitudinal range then expanded in both the poleward and equatorward directions with decreasing pressure until reaching its broadest latitudinal extent, typically at  $p=0.3$  to  $3$  Pa (e.g., Figures 7L and 6C, respectively). With further decreasing pressure, the poleward extent of PW was maintained while the equatorward extent retreated poleward such that at  $p < 0.1$  Pa PW rarely manifested below  $45^\circ$  latitude. During MY 29 and MY 30, the  $L_s=240$ – $300^\circ$  season (Figures 10A–10G and 13A–13F) exhibited a slightly different latitudinal structure, with both the poleward and equatorward extents shifting only poleward with decreasing pressure, resulting in a latitudinally narrow ( $\sim 10$ – $15^\circ$  in width) channel of PW. This is a consequence of the high-altitude  $T_2$ 's occurring at higher latitudes ( $\sim 60^\circ$ ) than at any other time throughout the year. As seen in the tables in the Supporting Information, there is not an absence of data at lower latitudes; however, as seen in Figure 2, the data are somewhat sparser during these seasons than some other seasons. At every season, the shape of the PW channel as a function of pressure and latitude is suggestive of a descending circulation branch that moves equatorward with increasing pressure, consistent with the circulation pattern proposed by McCleese et al. [2008]. The absence of

**Table 2.** Maximum Polar Warming Magnitudes Observed by MCS on the Nightside in the Southern Hemisphere During MY 28,  $L_s = 120^\circ \pm 5^\circ$

$p$ (Pa)	$\Delta_p T$ (K)	$T_1$ (K)	$\sigma_{T1}$ (K)	$Lat_{T1}$ ( $^\circ$ )	$T_2$ (K)	$\sigma_{T2}$ (K)	$Lat_{T2}$ ( $^\circ$ )	$z$ (km)	$\nabla_p T$ (K/ $^\circ$ )
5e-3									
1e-2									
5e-2	22	145	6.6	-85	123	7.5	-40	71	0.2
1e-1	27	154	6.4	-85	127	11.4	-40	65	0.2
5e-1	33	173	6.6	-75	140	6.0	-40	55	0.3
1e+0	39	174	4.9	-70	135	8.4	-5	50	0.5
5e+0	22	169	5.4	-65	147	4.4	-5	37	0.3
1e+1									
1.5e+0	43	174	4.4	-70	131	6.0	-5	47	0.6

The top eight rows show results for standard pressures interpolated by MCS. The bottom row shows results for the pressure at which PW maximizes in the southern hemisphere during this season. The quantities in each column are as follows: (1) pressure, (2)  $\Delta_p T$ , (3)  $T_1$ , (4)  $\sigma_{T1}$  (i.e., the standard deviation of temperatures about the longitudinal mean at  $Lat_{T1}$ ), (5) latitude of  $T_1$ , (6)  $T_2$ , (7)  $\sigma_{T2}$ , (8) latitude of  $T_2$ , (9) average altitude associated with the pressure in column 1 at  $Lat_{T1}$  and  $Lat_{T2}$ , and (10) the meridional temperature gradient associated with the PW.

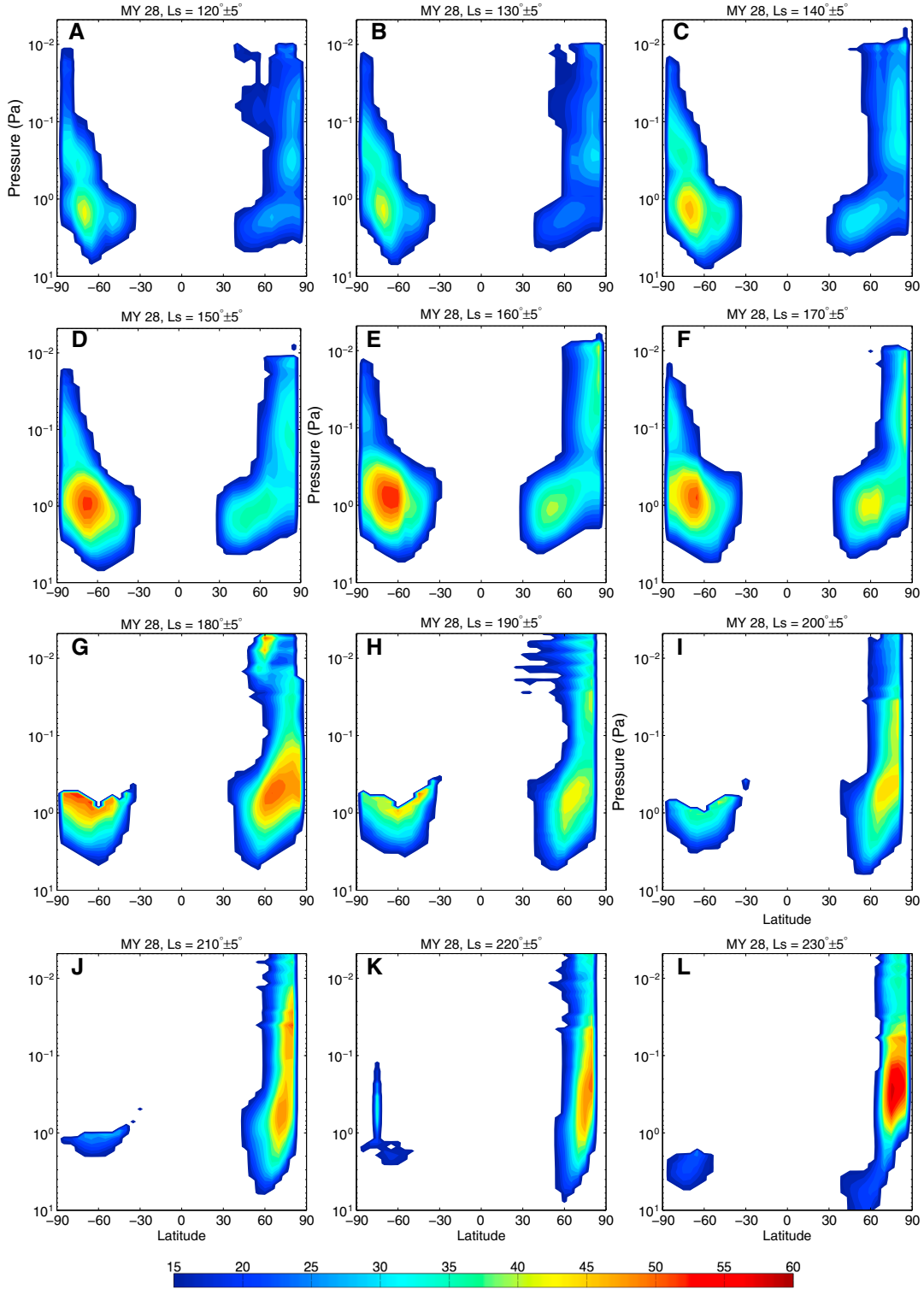


**Figure 6.** Vertical cross-sections of PW at  $10^\circ$ - $L_s$  intervals for MY 28. The color bar is in K. Contours are drawn every 2 K, beginning at 15 K.

high-latitude PW at the greatest pressures of manifestation is also consistent with the theory of Ferrel cells over the high latitudes of each hemisphere. Moreover, the latitudinal structure of the PW observed by MCS may suggest the Ferrel cell over the northern winter pole grows in height (i.e., extends to higher altitudes) from the time of the northern summer solstice until sometime postnorthern

winter solstice (e.g., Figure 6A through Figure 7A) and then shrinks in height with the approach of the summer solstice (e.g., Figure 7I through Figure 8I). This can be tested with future numerical simulations.

[28] The shape of the PW channel exhibited the most interannual variability during the early northern winter season. During MY 29 and MY 30, the early northern winter



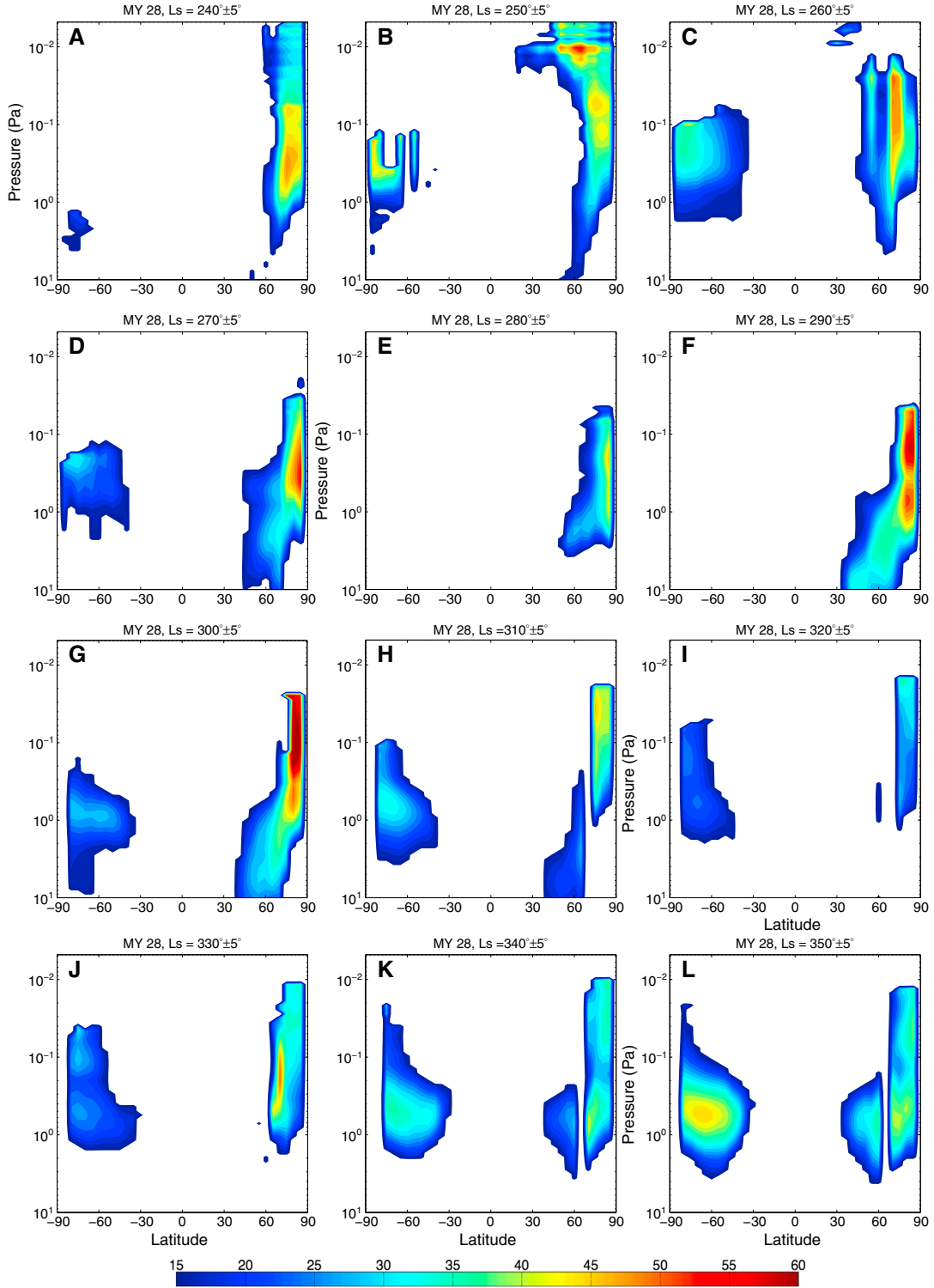
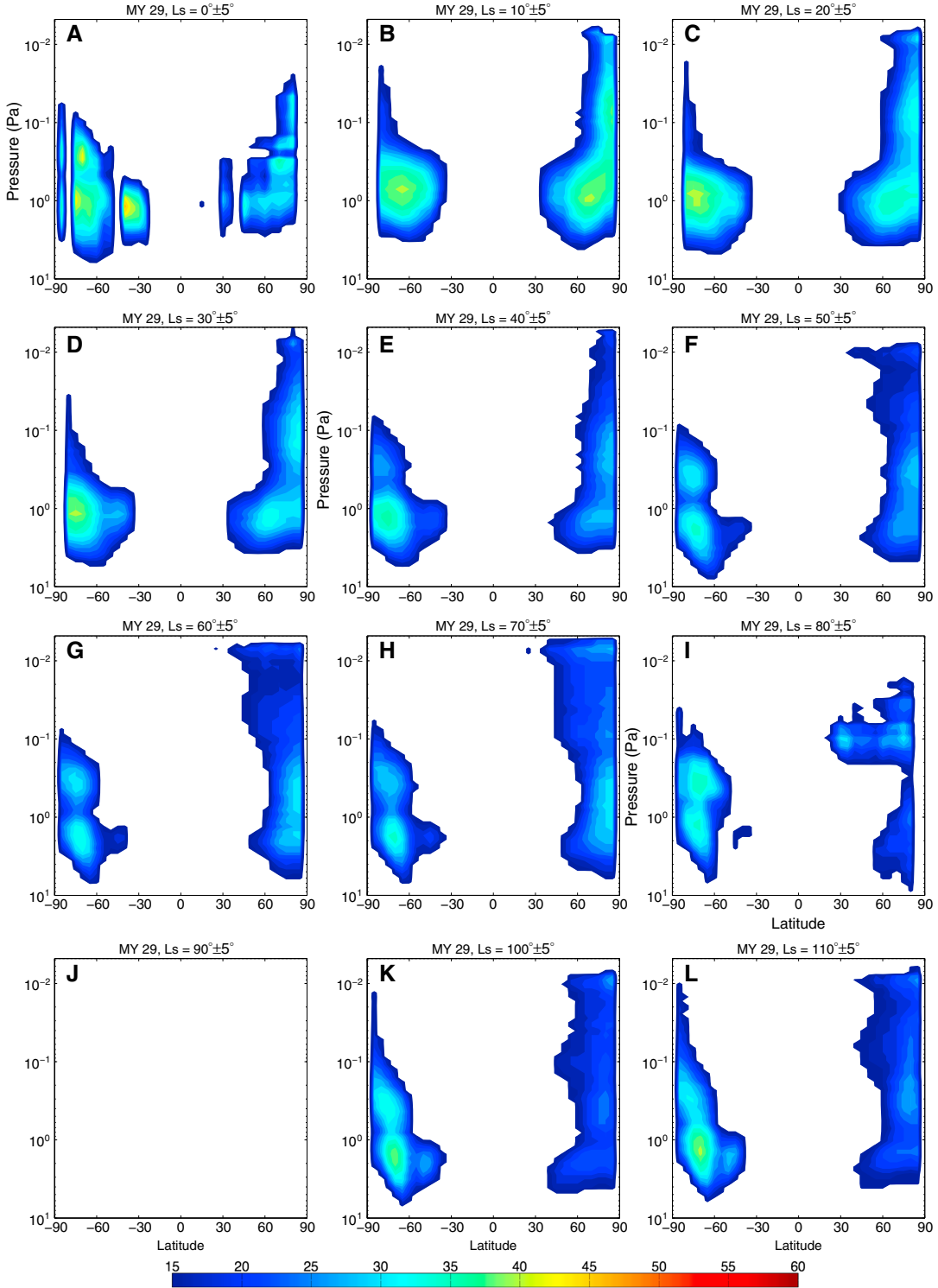


Figure 7. Continuation of Figure 6.

PW channel was narrow at all pressures and rarely extended below  $60^\circ$  latitude (Figures 10D–10H and 13D–13F) while during MY 28 the early northern winter PW channel was markedly broader and reached latitudes as low as  $45^\circ$  (Figures 7D–7H). This equatorward penetration during the period of the MY 28 global dust storm is consistent with the  $60^\circ$  north latitude position of the PW evident in Viking

IRTM temperatures observed during the initial stages of the early northern winter dust storm of MY 12 [Jakosky and Martin, 1987]. As seen in Figure 15, MY 28 experienced greater dust loading during the early northern winter than either MY 29 or MY 30. This may suggest that whatever process is responsible for suppressing the width of the PW channel during typical northern winters (i.e., those



**Figure 8.** Same as Figure 6, except for MY 29.

having regional but not global dust storms), is weakened during higher dust opacity conditions. Models can be used to test this hypothesis.

### 3.3. Maximum Magnitude of PW

[29] The maximum PW in the northern hemisphere varied from 28 K to 67 K (Figure 14a). The northern hemisphere annual maximum PW (53–67 K) occurred during northern

fall (MY 29 and MY 30) or winter (MY 28) (see Figure 14a). The observed northern winter solstice maximum values (37–56 K) are consistent with the wide range of previously modeled values ( $\sim 40$ –80 K) [Wilson, 1997; Forget *et al.*, 1999]. The observed northern-equinoctial maximum values (38–53 K), which frequently occurred near  $p = 0.5$  to 1 Pa (Figure 14b), are larger than those seen by TES, which found a maximum PW at the top of the TES domain

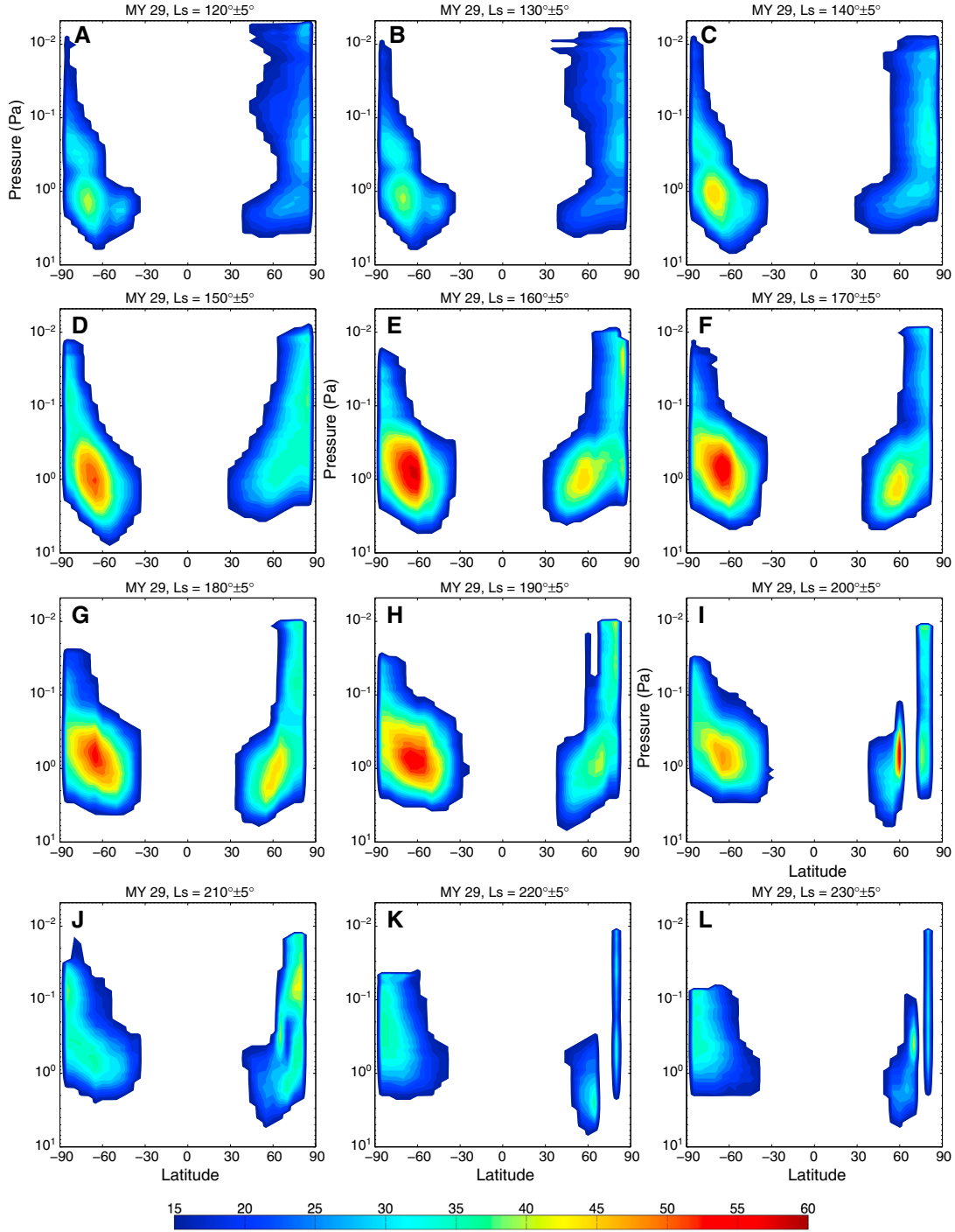


**Figure 9.** Continuation of Figure 8.

( $\sim 1$  Pa) of  $\sim 25$ – $30$  K during  $L_s = 180^\circ$  [Smith *et al.*, 2001]. The TES  $L_s = 180^\circ$  PW magnitude at 10 Pa exceeds the PW evident in Mariner 9 IRIS temperatures [Conrath, 1981] at  $L_s = 350^\circ$  also at 10 Pa. This fact is consistent with the preference for slightly larger maximum northern hemisphere PW at  $L_s = 180^\circ$  versus  $L_s = 350^\circ$  in the MCS observations (Figure 14a). The northern-equinoctial maximum PW values observed by MCS are also larger than indicated by previous modeling efforts ( $\sim 15$ – $25$  K) [Forget *et al.*, 1999].

[30] The maximum PW in the southern hemisphere varied from 22 K to 59 K (see Figure 14a). The southern hemisphere

annual maximum PW (51–59 K) occurred during late local winter to early local spring ( $L_s = 160$ – $180^\circ$ ) (see Figure 14a). The observed southern-winter maximum values are consistent with those seen by TES ( $\sim 40$  K) [Smith *et al.*, 2001] and consistent/larger than previously modeled values ( $\sim 10$ – $40$  K) [Forget *et al.*, 1999; Medvedev and Hartogh, 2007; Hartogh *et al.*, 2007]. Meanwhile, the values of the southern-equinoctial maximum PW (27–56 K), which generally occurred near  $p \sim 1$  Pa (Figure 14b), are larger than those seen by TES, which found a maximum PW at the top of the TES domain ( $\sim 1$  Pa) of  $\sim 30$  K during  $L_s = 180^\circ$ . The southern-equinoctial maximum

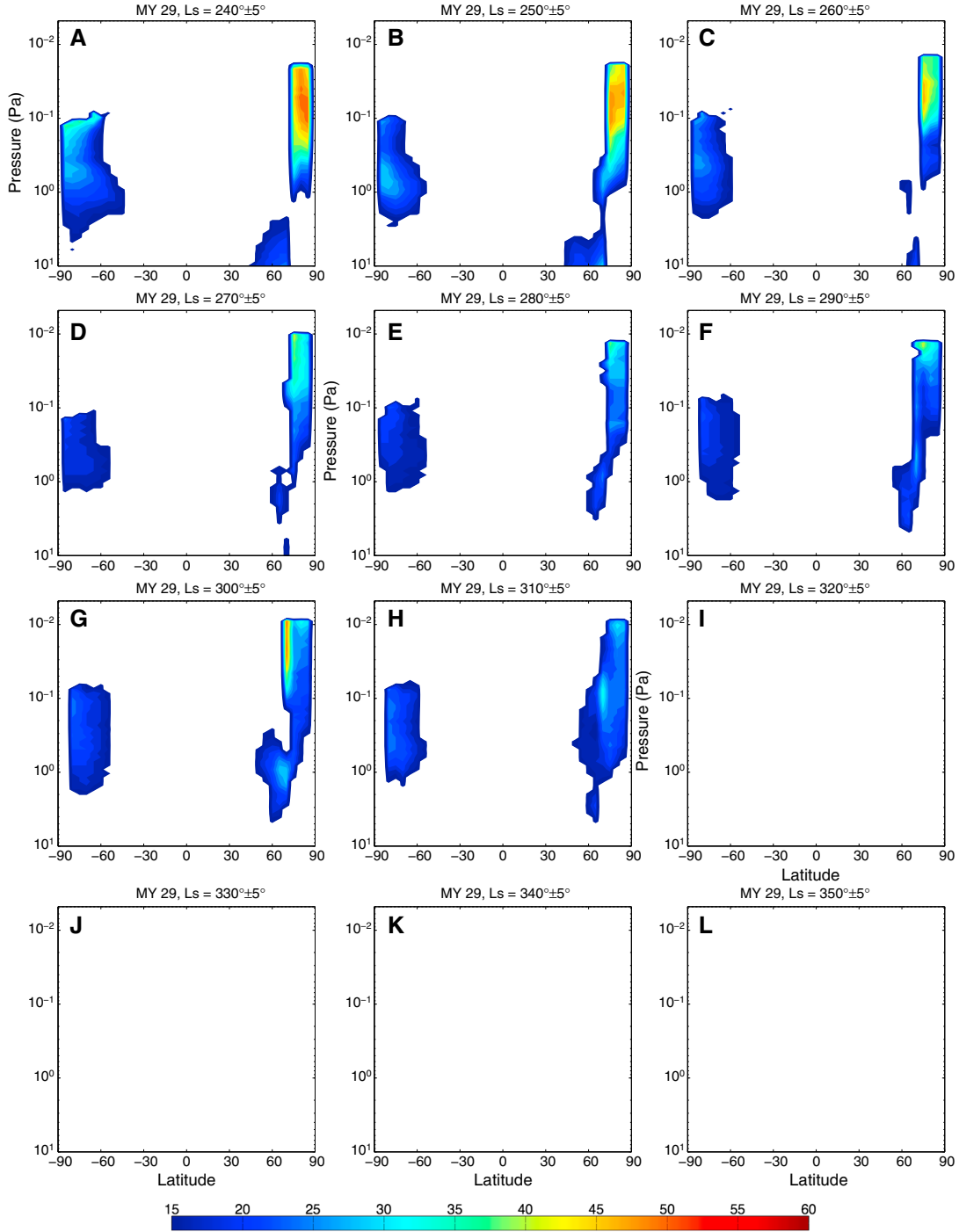


**Figure 10.** Continuation of Figure 9.

PW values observed by MCS are also larger than indicated by previous modeling efforts ( $\sim 15\text{--}25\text{ K}$ ) [Forget *et al.*, 1999].

[31] The northern winter solstice maximum PW was 12 K larger than the  $L_s = 120^\circ$  early southern winter maximum PW (see Figure 14a) in MY 28. This is consistent with previous studies that found dust-heating intensifies the overturning meridional circulation, which itself is at least partly responsible for PW. Curiously, however, the northern winter solstice maximum PW was comparable to the southern winter solstice maximum PW for both MY 29 and MY 30 (see Figure 14a), despite the northern winter solstices

having greater dust loading than the southern winter solstices (see Figure 15). Does this suggest that additional circulation components (gravity waves, tides, planetary waves) affect PW? Wind measurements and modeling experiments are needed to confirm or refute this hypothesis. Perhaps equally unexpectedly, most of the equinoxes observed by MCS exhibited southern-hemisphere maximum PW magnitudes that were 5–10 K larger than the simultaneous northern-hemisphere maximum PW magnitudes (compare, e.g., southern and northern PW magnitudes in Figures 8A, 9G, 11A, and 12G). The reason for this is not yet

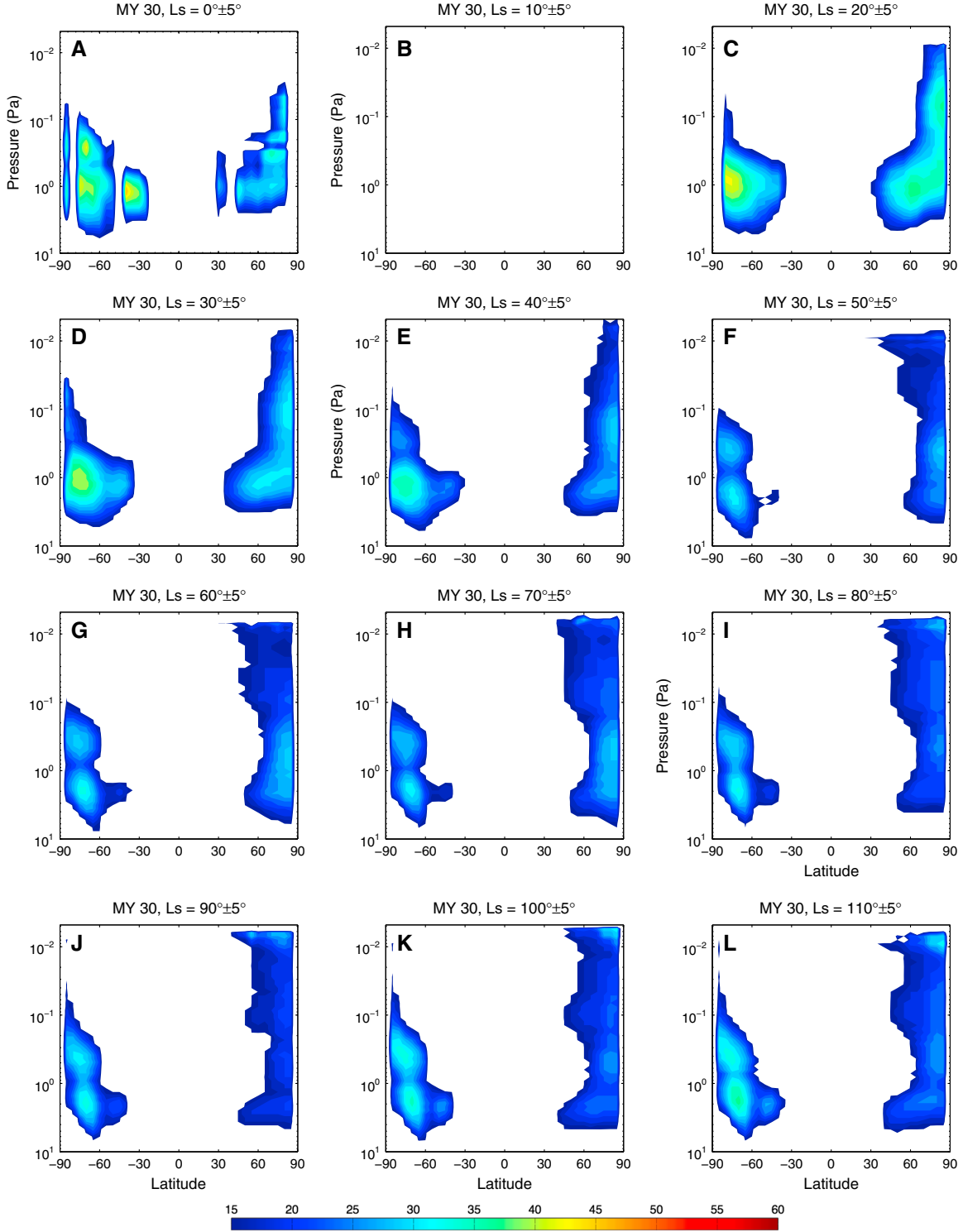


**Figure 11.** Same as Figure 6, except for MY 30.

clear. It may be symptomatic of a topographic influence as has been shown for the solstitial circulation [Richardson and Wilson, 2002]. Or perhaps the greater tidal forcing observed and modeled in the southern tropics [Bell *et al.*, 2007; Lee *et al.*, 2009; González-Galindo *et al.*, 2009a, 2009b] may explain this asymmetry. Further modeling studies are needed to understand the cause of this asymmetry. At any

rate, it seems to suggest an equinoctial circulation pattern that is asymmetric in strength about the equator.

[32] The pressure where the northern-hemisphere maximum PW occurred varied widely from  $p=0.005$  to 2.5 Pa (Figure 14b). The presence of high-altitude maxima during local fall and winter may be indicative of a connection between the MCS-observed middle-atmosphere PW

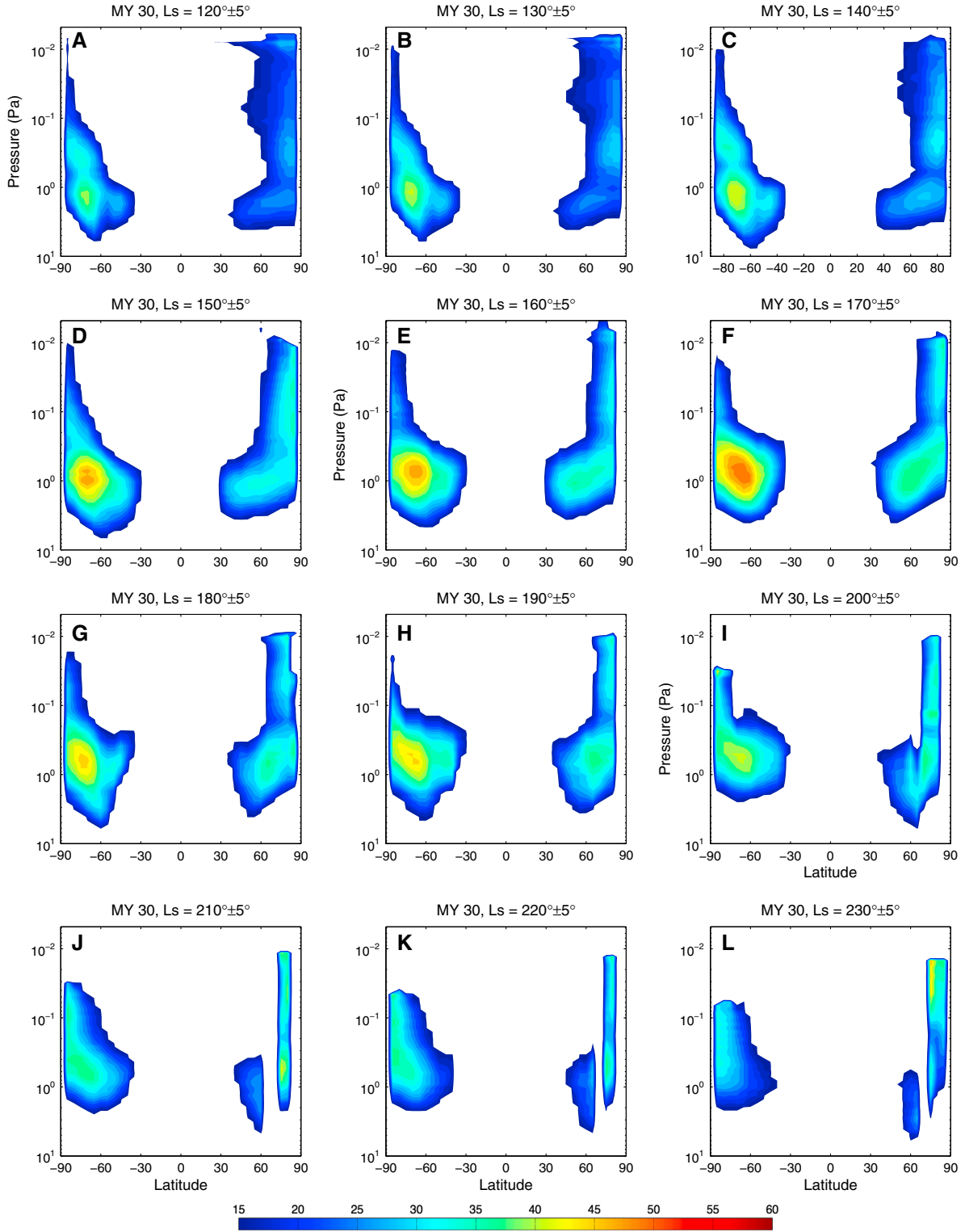


**Figure 12.** Continuation of Figure 11.

reported here and the thermospheric polar warming that has been observed by aerobraking spacecraft [e.g., *Bougher et al.*, 2006]. More consistent observations between 80 and 120 km are needed to determine this conclusively. We examined SPICAM observations and found their high-latitude coverage too sparse to identify significant PW features in this altitude range except during the southern

winter season, consistent with previously reported analyses of the SPICAM data [*Forget et al.*, 2009]. In general, the altitude where the MCS-observed northern-winter maximum PW occurred is consistent with or higher than previous GCM calculations indicated ( $\sim 40\text{--}70$  km) [*Wilson*, 1997; *Forget et al.*, 1999]. Additionally, the vertical location of the MCS-observed northern hemisphere maximum PW



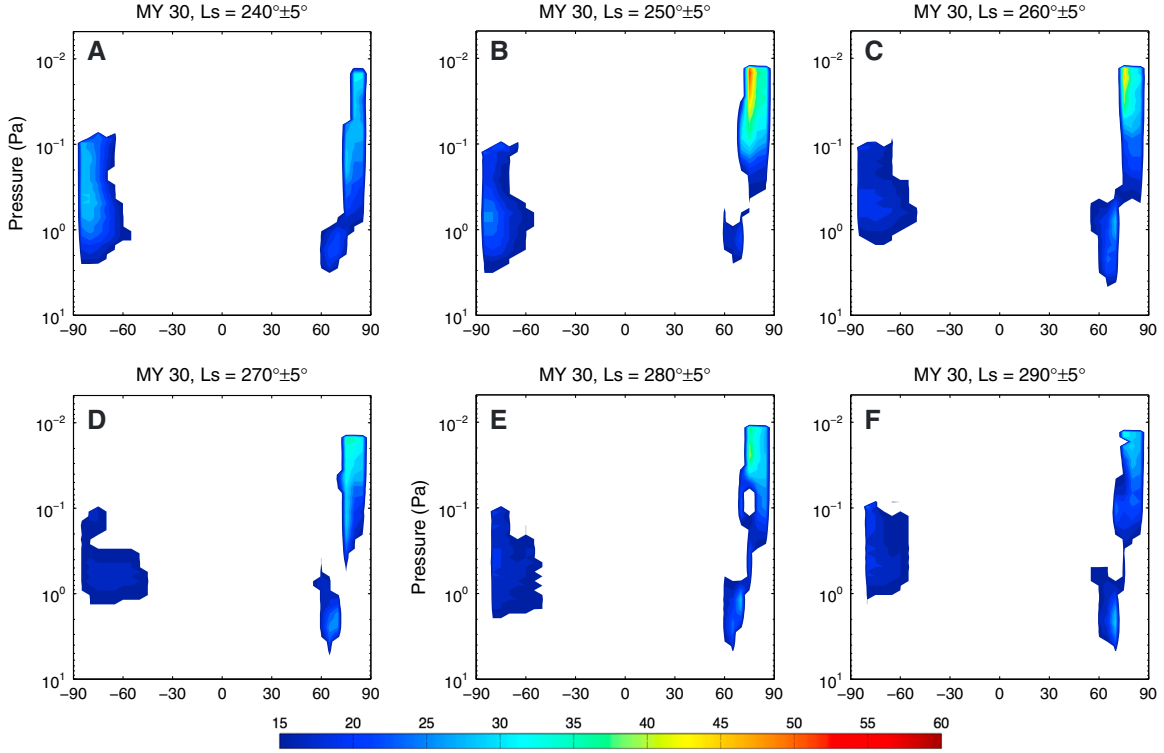


Figure 13. Continuation of Figure 12.

during  $L_s = 180^\circ$  is consistent with TES indications that PW maximized somewhere above the TES domain ( $\sim 1$  Pa) [Smith *et al.*, 2001].

[33] The pressure where the southern hemisphere maximum PW occurred varied from  $p = 0.03$  to 2 Pa (see Figure 14b). In general it occurred slightly lower in the atmosphere during local fall and winter, and slightly higher in the atmosphere during local spring (see Figure 14b). The southern winter solstice maximum PWs occurred lower in the atmosphere than previous calculations indicated ( $\sim 50$ – $80$  km) [Forget *et al.*, 1999; Medvedev and Hartogh, 2007; Hartogh *et al.*, 2007]. The vertical location of the southern hemisphere maximum PW during  $L_s = 180^\circ$  is consistent with TES indications that PW maximized somewhere above the TES domain ( $\sim 1$  Pa) [Smith *et al.*, 2001].

[34] The northern-winter maximum PW repeatedly occurred much higher in the atmosphere than the southern-winter maximum PW (see Figure 14b), perhaps suggesting that the descending branch of the meridional circulation does not penetrate as deep (i.e., as far downward) during northern winter. Modeling tests are needed to confirm this.

### 3.4. Dayside PW

[35] The PW features on the dayside (see the Supporting Information) tended to occur over smaller vertical and latitudinal ranges and have smaller magnitudes than those on the nightside. The largest night-day difference in northern-hemisphere maximum PW ( $\sim 12$ – $40$  K) occurred repeatedly during local fall through early-local winter and the largest night-day differences in southern hemisphere maximum PW ( $\sim 12$ – $25$  K) occurred repeatedly during late-local winter through early-local spring.

## 4. Middle-Atmosphere Constraints for GCMs

[36] Tables containing the bin-averaged MCS temperatures at  $5^\circ$  latitude intervals and half-decade intervals of log-pressure (see Table 3) are provided for both the nightside and the dayside at every  $10^\circ$  of  $L_s$  in the Supporting Information. These lookup tables can readily be used to validate middle-atmosphere GCM temperature calculations. In addition, the maximum PW features on each pressure surface have been tabulated at half-decade intervals of log-pressure for both the nightside and the dayside at every  $10^\circ$  of  $L_s$  and are provided in the Supporting Information. These tables contain pressure,  $\Delta_p T$ ,  $T_1$ ,  $\sigma_{T1}$  (i.e., the standard deviation of temperatures about the bin-average at  $Lat_{T1}$ ),  $Lat_{T1}$ ,  $T_2$ ,  $\sigma_{T2}$ ,  $Lat_{T2}$ , the average altitude associated with the pressure at  $Lat_{T1}$  and  $Lat_{T2}$ , and the meridional temperature gradient associated with the PW. These tables provide much-needed constraints for GCM calculations of unobserved wind fields in the middle atmosphere.

## 5. Summary

[37] In this paper we have characterized Martian middle-atmosphere PW based on nearly 3 Martian years of MCS temperatures. We have also provided tables of (1) bin-averaged temperatures as a function of latitude, pressure, and season, and (2) the maximum polar warming features on each pressure surface as a function of season. These tables provide the constraints needed for validation of middle-atmosphere GCM temperature calculations and constraint of middle-atmosphere wind calculations.

[38] Vertically, PW is observed between  $p = 1.1$  to 15 Pa and  $p = 4.8 \times 10^{-3}$  to  $1.0 \times 10^{-1}$  Pa and tends to manifest

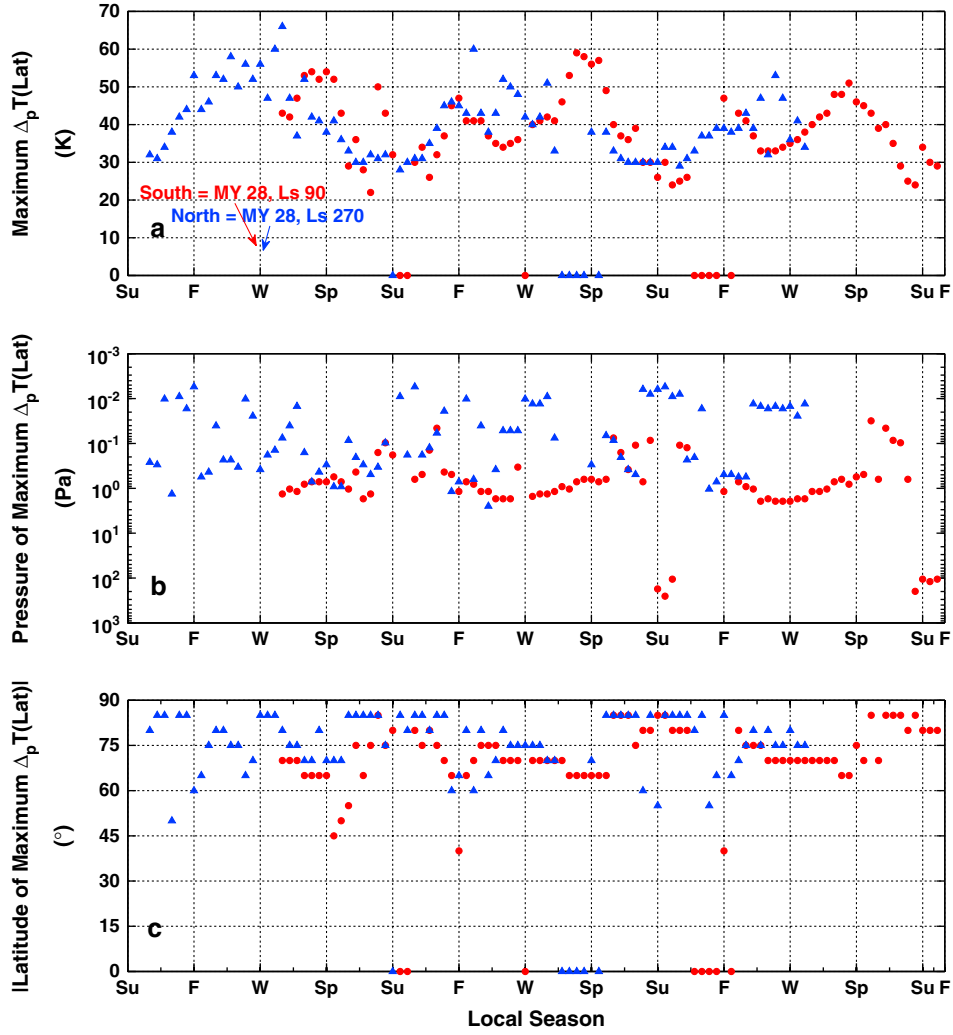


**Figure 14.** (a) Magnitude, (b) pressure, and (c) latitude of maximum nightside polar warming features as a function of local season in the southern hemisphere (red circles) and northern hemisphere (blue triangles). Note that the points in the two hemispheres are offset by  $180^\circ$  of  $L_s$  so that the local seasons in the two hemispheres are lined up and easily compared.

slightly lower in the atmosphere in the southern hemisphere and slightly higher in the atmosphere in the northern hemisphere. Latitudinally, PW is observed between  $\sim 25^\circ$  and  $85^\circ$  latitude. The pressure where PW maximizes varies widely with hemisphere and season from  $p=0.005$  to 2.5 Pa. In general northern-hemisphere maximum PW occurs higher in the atmosphere during local winter and

lower in the atmosphere during local fall and spring. Southern-hemisphere maximum PW, on the other hand, occurs slightly higher in the atmosphere during local spring and slightly lower in the atmosphere during local fall and winter. In the MCS observations, PW tends to be larger (by as much as 40 K) on the nightside than on the dayside. The maximum nightside PW magnitudes range from 22 to 67 K. As

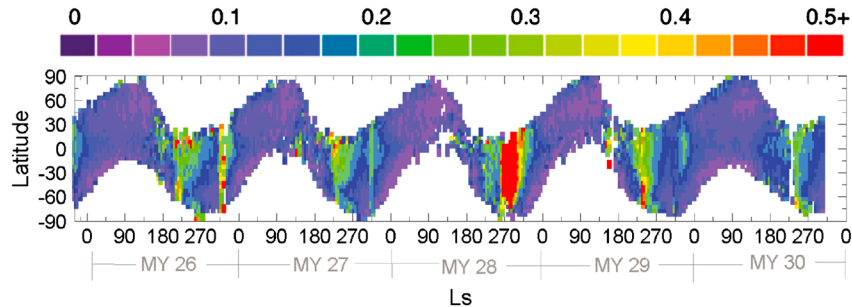


**Figure 15.** Dust optical depth ( $1075 \text{ cm}^{-1}$ ) scaled to 6.1 mbar surface as observed by Thermal Emission Imaging System (THEMIS) on board Mars Odyssey. Purple is  $\tau = 0.0$  and red is  $\tau \geq 0.5$ .

**Table 3.** Nightside Bin-Averaged MCS Temperatures on Select Pressure Surfaces at 5° Latitude Intervals. Southern Hemisphere. MY 28,  $L_s = 120^\circ \pm 5^\circ$ 

$p$ (Pa), Lat	−90	−85	−80	−75	−70	−65	−60	−55	−50	−45	−40	−35	−30	−25	−20	−15	−10	−5	0
5e−3																			
1e−2		132		120															
5e−2		145	142	134	133	129	126	124	126	127	123	129	131	131	131	131	133	129	134
1e−1		154	152	147	144	138	132	129	130	131	127	131	133	134	133	134	134	132	135
5e−1		164	169	173	173	170	163	154	146	142	140	140	141	143	144	146	146	145	143
1e+0		160	165	172	174	170	165	160	157	156	152	148	144	141	138	137	136	135	135
5e+0		136	141	152	163	169	165	160	157	154	153	152	151	150	149	148	148	147	147
1e+1		130	134	141	151	159	163	161	158	157	158	159	161	162	162	161	160	159	158

expected, the northern hemisphere annual-maximum PW occurred during late local fall to middle local winter. Perhaps unexpectedly, the southern hemisphere annual maximum PW occurred during late local winter. Another unexpected finding was that during MY 29 and MY 30, southern winter solstice and northern winter solstice had similar PW magnitudes, despite the greater dust opacity during the northern winter season. Yet another unanticipated finding was a hemispheric asymmetry in PW magnitude during most of the observed equinoxes.

[39] Further numerical investigation of the driving forces behind these hemispheric, diurnal, seasonal, and interannual variations in PW observed by MCS are needed. For example, GCM simulations conducted with and without topography influences may shed light on whether topographic asymmetry [e.g., *Richardson and Wilson*, 2002] is the driving force behind the asymmetric PW features observed during equinoxes. Another set of GCM simulations conducted with and without gravity wave influences can test whether gravity wave activity [e.g., *Medvedev and Hartogh*, 2007; *Medvedev et al.*, 2011] can account for the unexpected similarity in southern-winter and northern-winter PW magnitudes during MY 29 and MY 30. Finally, GCM simulations conducted with a variety of dust opacities and dust mixing depths can test which aspect of global dust storms led to the northern-winter PW channel broadening during MY 28 compared to MY 29 and MY 30.

[40] In addition to numerical investigations, further measurements are needed to determine the structure and magnitude of PW above the range of the MCS measurements. The anticipated MY 28 and MY 29 SPICAM observations may aid in this way. Measurements from the Mars Atmospheric and Volatile Evolution (MAVEN) mission (e.g., from the deep-dip accelerometer measurements, the Imaging Ultraviolet Spectrometer, and the Neutral Gas and Ion Mass Spectrometer [*Jakosky et al.*, 2012]) are also expected to improve the situation. Particularly exciting is the possibility for simultaneous upper atmosphere (MAVEN) and lower atmosphere (MCS) measurements (if both spacecraft are operating), which may shed light on the extension of the PW features from the lower to the upper atmosphere.

[41] **Acknowledgments.** We are grateful to Dan McCleese, Tim Schofield, and David Kass for access to the MCS dataset. We also would like to thank Alexander Medvedev and an anonymous reviewer for constructive comments that greatly improved the story and presentation of this paper. Finally, T.L.M. would like to acknowledge 3 years of funding from the NASA Earth and Space Science Fellowship.

## References

- Barnes, J. R. (1990), Possible effects of breaking gravity waves on the circulation of the middle atmosphere of Mars, *J. Geophys. Res.*, 95(B2), 1401–1421, doi:10.1029/JB095iB02p01401.
- Barnes, J. R., and J. L. Hollingsworth (1987), Dynamical modeling of a planetary wave mechanism for a martian polar warming, *Icarus*, 71, 313–334.
- Bell, J. M., S. W. Bougher, and J. R. Murphy (2007), Vertical dust mixing and the interannual variations in the Mars thermosphere, *J. Geophys. Res.*, 112(E12002), doi:10.1029/2006JE002856.
- Bertaux, J.-L., et al. (2006), SPICAM on Mars Express: Observing modes and overview of UV spectrometer data and scientific results, *J. Geophys. Res.*, 111(E10S90), doi:10.1029/2006JE002690.
- Bougher, S. W., J. M. Bell, J. R. Murphy, M. A. López-Valverde, and P. G. Withers (2006), Polar warming in the Mars thermosphere: Seasonal variations owing to changing insolation and dust distributions, *Geophys. Res. Lett.*, 33, doi:10.1029/2005GL024059.
- Conrath, B., R. Curran, R. Hanel, V. Kunde, W. Maguire, J. Pearl, J. Pirraglia, J. Welker, and T. Burke (1973), Atmospheric and surface properties of Mars obtained by infrared spectroscopy on Mariner 9, *J. Geophys. Res.*, 78(20), 4267–4278.
- Conrath, B. J. (1981), Planetary-scale wave structure in the martian atmosphere, *Icarus*, 48, 246–255.
- Denning, D., M. J. Mumma, F. Espenak, T. Kostiuik, and D. Zipoy (1986), Polar warming in the middle atmosphere of Mars, *JCARUS*, 66, 366–379.
- Forget, F., F. Hourdin, R. Fournier, C. Hourdin, O. Talagrand, M. Collins, S. R. Lewis, P. L. Read, and J.-P. Huot (1999), Improved general circulation models of the martian atmosphere from the surface to above 80 km, *J. Geophys. Res.*, 104, 24,155–24,176, doi:10.1029/1999JE001025.
- Forget, F., F. Montmessin, J.-L. Bertaux, F. Gonzalez-Gálindo, S. Lebonnois, E. Quémerais, A. Reberac, E. Dimarellis, and M. A. López-Valverde (2009), Density and temperatures of the upper martian atmosphere measured by stellar occultations with Mars Express SPICAM, *J. Geophys. Res.*, 114(E01004), doi:10.1029/2008JE003086.
- González-Galindo, F., F. Forget, M. A. López-Valverde, M. Angelats i Coll, and E. Millour (2009a), A ground-to-exosphere martian general circulation model: 1. Seasonal, diurnal, and solar cycle variation of thermospheric temperatures, *J. Geophys. Res.*, 114(E04001), doi:10.1029/2008JE003246.
- González-Galindo, F., F. Forget, M. A. López-Valverde, and M. Angelats i Coll (2009b), A ground-to-exosphere martian general circulation model: 2. Atmosphere during solstice conditions - Thermospheric polar warming, *J. Geophys. Res.*, 114(E08004), doi:10.1029/2008JE003277.
- Hartogh, P., A. S. Medvedev, and C. Jarchow (2007), Middle atmosphere polar warmings on Mars: Simulations and study on the validation with sub-millimeter observations, *Plan. and Space Sci.*, 55, 1103–1112, doi:10.1016/j.pss.2006.11.018.
- Heavens, N. G., M. I. Richardson, W. G. Lawson, D. J. McCleese, D. M. Kass, A. Kleinböhl, J. T. Schofield, W. A. Abdou, and J. H. Shirley (2010), Convective instability in the martian middle atmosphere, *JCARUS*, 208, 574–589, doi:10.1016/j.icarus.2010.03.023.
- Heavens, N. G., D. J. McCleese, M. I. Richardson, D. M. Kass, A. Kleinböhl, and J. T. Schofield (2011), Structure and dynamics of the martian lower and middle atmosphere as observed by the Mars Climate Sounder: 2. Implications of the thermal structure and aerosol distributions for the mean meridional circulation, *J. Geophys. Res.*, 116(E01010), doi:10.1029/2010JE003713.
- Holton, J. R. (1982), The role of gravity wave induced drag and diffusion in the momentum budget of the mesosphere, *J. Atmos. Sci.*, 39, 791–799.
- Jakosky, B. M., and T. Z. Martin (1987), Mars: North-polar atmospheric warming during dust storms, *Icarus*, 72, 528–534.

- Jakosky, B. M., J. Grebowsky, and D. Mitchell (2012), The 2013 Mars Atmospheric and Volatile Evolution (MAVEN) Mission, in *25th Mars Exploration Program Analysis Group* (<http://mepag/meeting/feb-12/index.html>), Washington, D.C.
- Keating, G. M., M. E. Theriot, R. H. Tolson, S. W. Bougher, F. Forget, M. Angelats i Coll, and J. M. Forbes (2003), Recent detection of winter polar warming in the Mars upper atmosphere, in *The Third International Mars Polar Science Conference*, pp. 8033–+, Pasadena, California.
- Kellogg, W. W., and G. F. Schilling (1951), A proposed model of the circulation in the upper stratosphere, *J. Meteorology*, **8**, 222–230.
- Kleinböhl, A., et al. (2009), Mars Climate Sounder limb profile retrieval of atmospheric temperature, pressure, and dust and water ice opacity, *J. Geophys. Res.*, **114**(E10006), doi:10.1029/2009JE00358.
- Kleinböhl, A., J. T. Schofield, W. A. Abdou, P. G. J. Irwin, and R. J. de Kok (2011), A single-scattering approximation for infrared radiative transfer in limb geometry in the martian atmosphere, *J. Quant. Spectrosc. Radiat. Transfer*, **112**, 1568–1580, doi:10.1016/j.jqsrt.2011.03.006.
- Kuroda, T., A. Medvedev, P. Hartogh, and M. Takahashi (2009), On forcing the winter polar warmings in the martian middle atmosphere during dust storms, *J. Meteorol. Soc. Japan*, **87**, 913–921, doi:10.2151/jmsj.87.913.
- Lee, C., et al. (2009), Thermal tides in the martian middle atmosphere as seen by the Mars Climate Sounder, *J. Geophys. Res.*, **114**(E03005), doi:10.1029/2008JE003285.
- Leovy, C. B. (1964), Simple models of thermally driven mesospheric circulations, *J. Atmos. Sci.*, **21**, 327–341.
- Martin, T. Z., and H. H. Kieffer (1979), Thermal infrared properties of the martian atmosphere 2. The 15-  $\mu$  m band measurements, *J. Geophys. Res.*, **84**(B6), 2843–2852.
- McCleese, D. J., et al. (2007), Mars Climate Sounder: An investigation of thermal and water vapor structure, dust and condensate distributions in the atmosphere, and energy balance of the polar regions, *J. Geophys. Res.*, **112**(E05S06), doi:10.1029/2006JE002790.
- McCleese, D. J., et al. (2008), Intense polar temperature inversion in the middle atmosphere on Mars, *Nature Geoscience*, **1**, 745–749, doi:10.1038/ngeo332.
- McCleese, D. J., et al. (2010), The structure and dynamics of the martian lower and middle atmosphere as observed by the Mars Climate Sounder: Seasonal variations in zonal mean temperature, dust and water ice aerosols, *J. Geophys. Res.*, **115**(E12016), doi:10.1029/2010JE003677.
- McDunn, T. L., S. W. Bougher, J. Murphy, M. D. Smith, F. Forget, J.-L. Bertaux, and F. Montmessin (2010), Simulating the density and thermal structure of the middle atmosphere (80–130 km) of Mars using the MGCM-MTGCM: A comparison with MEX/SPICAM observations, *ICARUS*, **206**, 5–17, doi:10.1016/j.icarus.2009.06.034.
- Medvedev, A., E. Yigit, and P. Hartogh (2011), Estimates of gravity wave drag on Mars: Indication of a possible lower thermospheric wind reversal, *Icarus*, **211**, 909–912, doi:10.1016/j.icarus.2010.10.013.
- Medvedev, A. S., and P. Hartogh (2007), Winter polar warmings and the meridional transport on Mars simulated with a general circulation model, *ICARUS*, **186**, 97–110, doi:10.1016/j.icarus.2006.08.020.
- Montmessin, F., et al. (2006), Subvisible  $\text{CO}_2$  ice clouds detected in the mesosphere of Mars, *Icarus*, **183**, 403–410, doi:10.1016/j.icarus.2006.03.015.
- Quémerais, E., J.-L. Bertaux, O. Korablev, E. Dimarellis, C. Cot, B. R. Sandel, and D. Fussen (2006), Stellar occultations observed by SPICAM on Mars Express, *J. Geophys. Res.*, **111**(E09S04), doi:10.1029/2005JE002604.
- Richardson, M. I., and R. J. Wilson (2002), A topographically forced asymmetry in the martian circulation and climate, *Nature*, **416**, 298–301.
- Santee, M., and D. Crisp (1993), Thermal structure and dust loading of the martian atmosphere during late southern summer: Mariner 9 revisited, *J. Geophys. Res.*, **98**(E2), 3261–3279.
- Schneider, E. K. (1983), Martian great dust storms: Interpretive axially symmetric models, *ICARUS*, **55**, 302–331.
- Smith, M. D., J. C. Pearl, B. J. Conrath, and P. R. Christensen (2001), Thermal Emission Spectrometer results: Mars atmospheric thermal structure and aerosol distribution, *J. Geophys. Res.*, **106**(E10), 23,929–23,945, doi:10.1029/2000JE001321.
- Théodore, B., E. Lellouch, E. Chassefière, and A. Hauchecorne (1993), Solstitial temperature inversions in the martian middle atmosphere: Observational clues and 2-D modeling, *ICARUS*, **105**, 512–528.
- Tolson, R. H., G. Keating, R. Zurek, S. Bougher, C. Justus, and D. Fritts (2007), Application of accelerometer data to atmospheric modeling during Mars aerobraking operations, *J. Spacecraft and Rockets*, **44**(6), 1172–1179, doi:10.2514/1.28472.
- Wilson, R. J. (1997), A general circulation model simulation of the martian polar warming, *Geophys. Res. Lett.*, **24**(2), 123–126.